Experiments on helicon plasma sources

Francis F. Chen
University of California, Los Angeles, California 90024-1594

(Received 25 September 1991; accepted 16 December 1991)

This work concerns a search for novel plasma generators with applications to materials processing and advanced accelerators and radiation sources. Experimental measurements, together with a summary of the theory, are presented on the production of high-density plasmas using radio-frequency (rf) excitation of helicon waves. Plasma densities above 3×10^{13} cm^{-3} have been achieved with 2 kW of rf power. The required power agrees with classical diffusion theory. The scaling of density with magnetic field agrees with the theory of helicon waves. The effect of different antenna designs is demonstrated. Unexpected observations include: (a) a density maximum occurring at very low magnetic fields, (b) an increase in peak density with nonuniform fields, and (c) the strong effects of dc wall potentials on the behavior of the discharge. Tentative explanations of these phenomena are presented.

I. INTRODUCTION

As future alternatives to the capacitive discharge and electron cyclotron resonance (ECR) plasma sources for materials processing, we are interested in radio-frequency (rf) discharges at 13.56 MHz and its related frequencies of 27.12 and 6.78 MHz. Though interesting discharges can be produced by nonresonant helical antennas, we have been attracted to the helicon wave discharge developed by Boswell and co-workers,[1–5] because this type of discharge has been shown to have unusually high ionization efficiency, does not require internal electrodes or large sheath voltages, and offers a possible means of controlling the electron velocity distribution. In an ordinary gas discharge, ionizing electrons are accelerated past the ionization threshold (15.7 eV in argon) to an optimum energy of 50–100 eV (in argon), either in a cathode sheath or in an electric field in the body of the plasma. During the acceleration and after each ionization event, a primary electron finds itself in an energy range where the cross section for the excitation of spectral lines far exceeds that for ionization, and it loses energy to inelastic collisions. Consequently, it normally requires more than ten times the ionization energy, or about 200 eV, to produce each electron-ion pair. Helicon discharges are an order of magnitude more dense for given input power. We believe that the reason for this efficiency is that primary electrons are produced by trapping and acceleration of electrons in a helicon wave, which can quickly bring them to the optimum energy and reaccelerate them to that energy after each ionization event. Of all the waves possible in a plasma, helicon waves fortuitously have a phase velocity of the right magnitude to do this.

Absorption of plasma wave energy by acceleration of particles is known as Landau damping. We have calculated the damping rate due to thermal distribution of electrons,[6] and our theoretical predictions have been verified by both Shoji's group[7] and Boswell's group.[8] The damping rate due to acceleration of fast electrons, forming a tail in the distribution, depends on the trapping efficiency and is best investigated experimentally. The work reported here is a first step in the understanding of how helicon and other rf discharges work, with the ultimate goal of controlling the electron distribution and the production of various molecular ion species.

In addition to plasma processing, helicon discharges are also useful as targets in plasma-based particle accelerator devices and coherent radiation generators, as plasma generators in experiments on wall and edge effects in magnetic fusion reactors, and as plasma sources for large-volume experiments on ionospheric and magnetospheric plasma physics. We have so far used quartz tubes of two diameters: 2 cm for accelerator applications, and 4 cm as a step toward the larger radii suitable for the other applications. Even these diameters have given unanticipated results showing the complexity of rf discharges. Although we have previously pointed out the important role of the electrostatic component of the rf field,[6] we did not expect that the dc electrostatic fields on the walls would govern the behavior of such plasmas. A principal result of the work reported here is the evidence for these electrostatic effects.

II. THEORETICAL EXPECTATIONS

A. Dispersion relation

A helicon wave is the same as an ionospheric whistler wave except for two differences: the frequency is much lower, and the wave is bounded by a cylinder. The well known whistler wave dispersion relation is

$$\frac{c^2k^2}{\omega^2} = 1 - \frac{\omega_p^2}{\omega(\omega - \omega_c \cos\theta)}, \tag{1}$$

where ω is its angular frequency, k its wave number, $\omega_p = (ne^2/\epsilon_0 m)^{1/2}$ the plasma frequency, n the plasma density, $\omega_c = eB/m$ the electron cyclotron frequency in the uniform background magnetic field B, and θ the angle of k relative to B. At sufficiently low frequency, the first term in the denominator can be neglected, as well as the "1," which represents the displacement current. In this approximation, the oscillating current in the wave is carried by the guiding-center motion of the electrons, their cyclotron gyrations being too fast to matter. Equation (1) then becomes

 0734-2101/92/041389-13$01.00

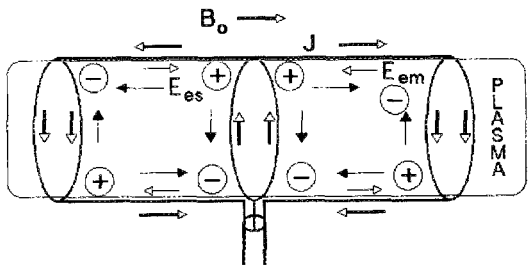

Nagoya Type III Antenna
(m = 1)

FIG. 1. Physical mechanism of the Nagoya type III antenna. A full wavelength antenna is pictured here; half of such an antenna is used in the experiment.

$$\frac{c^2k^2}{\omega^2}=\frac{\omega_p^2}{\omega\omega_c\cos\theta}. \tag{2}$$

In a confined plasma, the square of the total wave number k^2 is the sum of $k_\perp^2$ and $k_\parallel^2$, where $k_\parallel/k$ is $\cos\theta$, and the finite value of $k_\perp$ is set by the boundary conditions. For a cylinder of radius a aligned with **B**, the lowest radial mode has $k_\perp$ approximately equal to p_{11}/a, where $p_{11}=3.83$ is the first zero of the Bessel function $J_1(k_\perp r)$. Equation (2) can then be written

$$k=\frac{\omega}{k_\parallel}\frac{\omega_p^2}{\omega_c c^2}=e\mu_0 v_p\left(\frac{n}{B}\right)\approx\frac{3.83}{a}, \tag{3}$$

where $v_p=\omega/k_\parallel$ is the wave's phase velocity along the tube. Since the optimum value of v_p is presumably fixed by the Landau damping mechanism, Eq. (3) shows that the helicon resonance requires na/B to be a constant. For each given radius a, the density n should vary linearly with B; and for given n, the required field B should vary linearly with tube radius a. Since $v_p=\omega/k_\parallel$, the rf frequency does

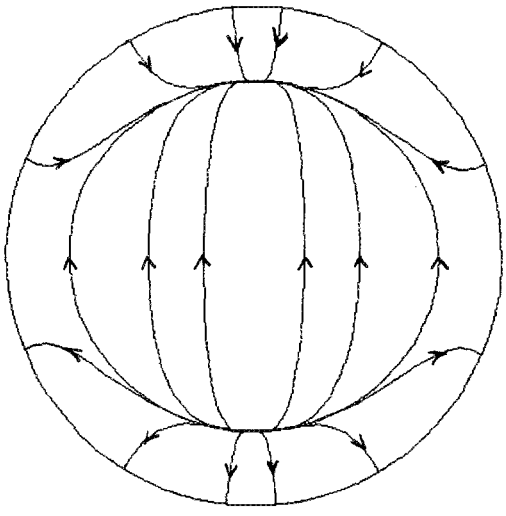

FIG. 2. Electric field lines in an $m=1$ helicon wave.

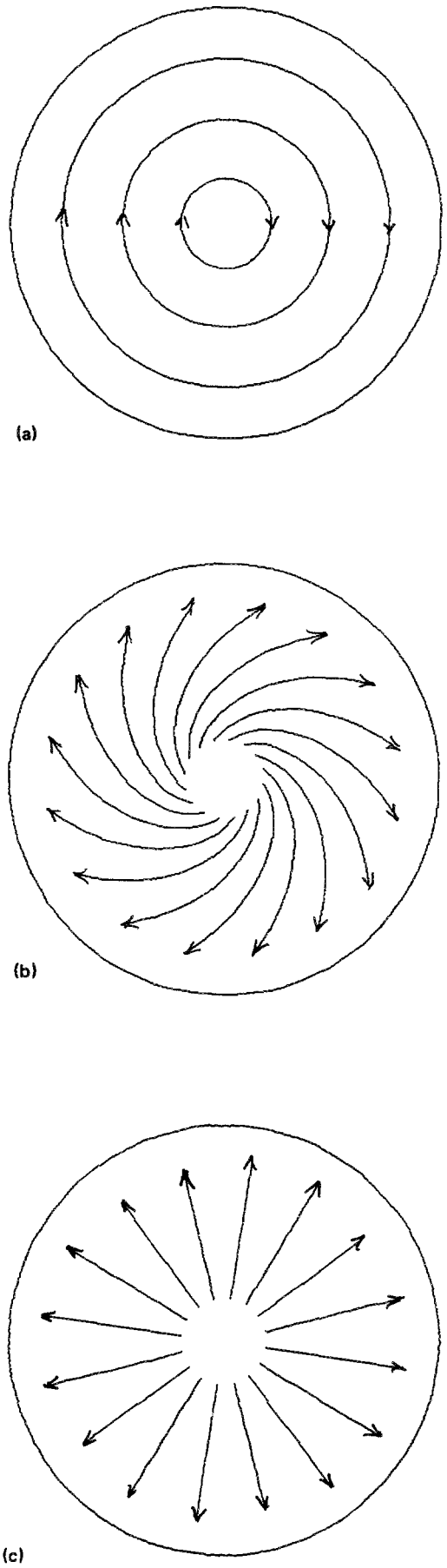

FIG. 3. Electric field lines in an $m=0$ helicon wave at three cross sections, where (a) and (c) are a quarter wavelength apart.

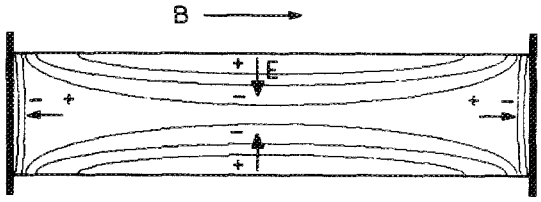

FIG. 4. Schematic of a generic cylindrical discharge in a magnetic field. The qualitative configuration of dc equipotential contours is shown, but whether these contours are concentrated in thin sheaths or extended throughout the discharge depends on the conductivity of the walls and the electron distributions in the plasma.

not matter as long as $k_\parallel$ can be adjusted to give the right v_p; however, antenna coupling considerations discussed below will tie $k_\parallel$ to $k_\perp$, so that a larger radius a will call for smaller $k_\perp$ and $k_\parallel$, and hence smaller operating frequency ω (cf. Ref. 6).

B. Antenna coupling

Our studies have been made with antennas designed to excite the $m = 1$ mode, where m is the azimuthal mode number. We normally use a Nagoya type III configuration,[9] shown schematically in Fig. 1. The high efficiency of this antenna can be understood as follows. The current in the horizontal legs of the antenna, parallel to **B**, are the important ones; the vertical legs simply provide a return path. Since the antenna length is much smaller than the free-space wavelength of the rf signal, the current pattern is established almost instantaneously. Consider a time when the current J in Fig. 1 is rising in the direction shown. The rising magnetic field induces a divergence-free electric field E_{em} in the plasma. Since the antenna has a finite $k_\parallel$, E_{em} reverses sign periodically in the z direction. This causes a momentary electron flow which creates a space charge pattern, as indicated by the + and − signs. The space charge, in turn, creates a curl-free electric field E_{es}, shown by the solid arrows, which builds up until the total electric field parallel to **B**, $E_{em} + E_{es}$, is nearly zero, which it must be in a highly conducting plasma. For an $m = 1$ configuration, these currents and space charges are of opposite polarity on the top and bottom of the plasma.

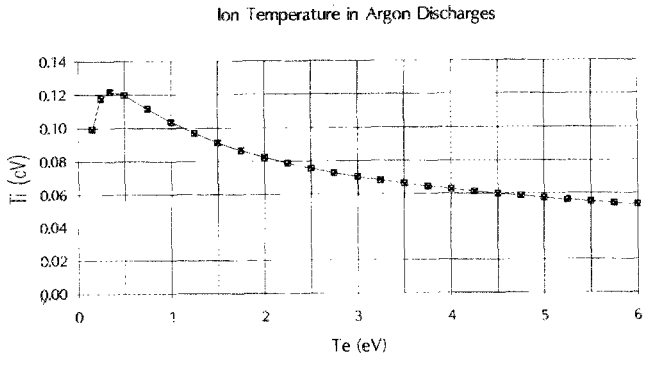

FIG. 5. Calculated ion temperature vs T_e in 10% ionized argon discharges.

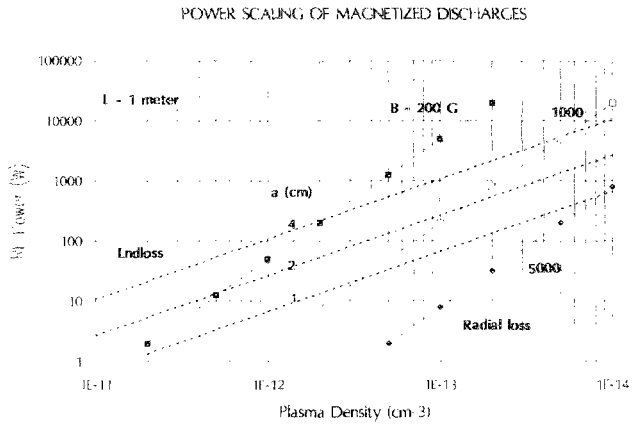

FIG. 6. Predicted scaling of rf power with density in the case of (a) axial loss only (dashed curves, for various values of tube radius a in cm) and (b) radial loss only (solid curves, for various values of B in Gauss. A discharge length of 1 m is assumed.

As a result, there is also a perpendicular component of $\mathbf{E}_{es}$, which is in the same direction as the E_{em} induced by the rising current in the perpendicular legs, but is much larger. There is therefore an enhancement of the induced electric field because of the electrostatic charges. The amplification factor has been calculated by Chen[10] for plane geometry to be $(k_\perp^2/k_\parallel^2)$ and by McVey[11] for cylindrical geometry to be, equivalently $(p_{11}/ak_\parallel)^2$.

Since the electrostatic field has its source in internal space charges, it is not shielded out, extends through the center of the plasma, and couples strongly to the electrostatic field of the helicon wave. This field pattern is shown in Fig. 2, taken from Ref. 6. The straight field lines near the axis are due to electrostatic charges near the separatrix, and therefore can be expected to couple efficiently to the similar electrostatic field pattern excited by the $m = 1$ antenna. The dominance of the electrostatic component of the helicon E field can be appreciated from the fact that an electromagnetic wave in a vacuum waveguide has a *magnetic* field pattern which looks exactly like Fig. 2, except for a small change in the location of the separatrix. The presence of the plasma has caused the roles of the electric and magnetic fields to be interchanged.

The antenna pictured in Fig. 1 would excite a plane-polarized wave. The whistler in free space is right-hand circularly polarized, and one would think that a helical antenna would couple better to such a wave. We have found, however, that helicon waves, because of the boundaries, have both right- and left-handed versions which should propagate equally well, albeit with slightly different dispersion relations. By adding left- and right-hand polarized helicons, we have been able to show that nearly plane-polarized helicons are possible,[12] so that it should not be necessary to use helical antennas.

The field pattern for $m = 0$ helicons is shown in Fig. 3. In successive half wavelengths, the electric field changes from pure electromagnetic [Fig. 3(a)] to pure electrostatic [Fig. 3(b)]. The antennas used to produce these waves can be circular hoops with currents alternating in direction every half wavelength. Though a calculation has not yet

been made, it should be possible to couple electrostatically to this pattern also. A current in the ring antenna would induce an azimuthal electric field like that in Fig. 3(a). The electrons cannot move in the direction of E because they are magnetized; instead, they perform an $E\times B$ drift in the radial direction. This causes a space charge to build up near the axis, resulting in an electrostatic field like that in Fig. 3(b). Thus, the antenna can couple to the helicon field during its electrostatic half cycle; the E field produced by the antenna is perpendicular to that which it would produce in a vacuum.

C. Confinement scaling

We now calculate the power necessary to sustain rf discharges in magnetic fields strong enough to magnetize the electrons but not the ions. The electrons are then confined radially by the magnetic field and axially by sheath electric fields where the magnetic field lines intersect the walls. The ions are confined radially by an ambipolar electric field but are not confined axially at all; they are lost by streaming along the magnetic field at the acoustic velocity. This generic configuration is shown in Fig. 4. It is well known[13] that diffusion in such a system is not separable in the r and z directions, and, furthermore, the diffusion problem is nonlinear if it is dominated by electron–ion collisions. Nonetheless, we can obtain reasonable estimates by calculating the radial and axial losses separately.

1. Axial loss only

If the discharge is short or the magnetic field is strong, radial losses can be neglected; and the plasma is lost by ambipolar diffusion to the ends. The loss rate is then controlled by the ions. Though the ions collide with electrons more often than with neutral atoms, there is no friction against the comoving electron fluid, and the ambipolar diffusion coefficient D_a can be calculated using the argon charge-exchange cross section. Let the ionization source be proportional to electron density, as would be the case if the primary electron fraction is constant, and let the constant of proportionality be Q. The steady-state continuity equation is then

$$D_a\frac{\partial^2 n}{\partial z^2}+Qn=0, \tag{4}$$

with the solution[13] $n=n_0\cos kz$, where $k=(Q/D_a)^{1/2}$. At the sheath edge, the ions must satisfy the Bohm condition and therefore have a drift velocity of the order of the acoustic velocity, given, for $T_i \ll T_e$, by

$$c_s=(kT_e/M)^{1/2}. \tag{5}$$

Let the endplates be at $z=\pm L$. The ion flux $-D_a(\partial n/\partial z)$ there must be matched to $\pm n(\pm L)c_s$. This gives the following equation for k:

$$k\tan kL=c_s/D_a. \tag{6}$$

If W is the energy in eV that has to be expended to produce each ion–electron pair, the power P needed to sustain the plasma is

$$P=eW(2\pi a^2)Q\int_{-L}^{L} n_0\cos kz\,dz=2(2\pi a^2)eWkD_an_0, \tag{7}$$

where a is the plasma radius. Taking $c_s\approx 2.8\times 10^3$ m/s ($KT_e=3$ eV, argon), $W\approx 200$ eV, $n_{13}=n$ in units of 10^{13} cm^{-3}, $a_{\rm cm}=a$ in cm, and $kL\simeq\pi/2$, we can approximate P by

$$P\simeq 3500(a^2/L)_{\rm cm}n_{13}\ \text{W}.$$

Thus, for $a=5$ cm and $L=50$ cm, 1.75 kW is needed to produce a density of 10^{13} cm^{-3}. Since Boswell *et al.*[1] observed densities an order of magnitude higher under these conditions, either the density was peaked so that the effective radius was smaller than the tube radius, or the helicon wave mechanism was able to reduce W well below its usual value. Equation (7) shows that axial losses decrease with the length of the discharge and depend linearly on the density and the cross sectional area.

2. Radial loss only

Because our experiments span a large range of magnetic fields and densities, no single model for radial losses can be used. As a starting point, we first consider cross-field diffusion due to momentum-changing collisions at some unspecified frequency ν. The steady-state continuity equation is then

$$D_\perp\nabla_\perp^2 n+Qn=0,\quad \frac{\partial^2 n}{\partial r^2}+\frac{1}{r}\frac{\partial n}{\partial r}+\frac{Q}{D_\perp}n=0, \tag{8}$$

where, for the moment, we have taken the cross-field diffusion coefficient $D_\perp$ to be constant. The lowest Bessel function solution is

$$n=n_0J_0(\kappa r),\quad \text{where}\quad \kappa=(Q/D_\perp)^{1/2}=2.4/a. \tag{9}$$

The power required to supply these losses is

$$P=2\pi eWQL\int_0^a rn(r)dr. \tag{10}$$

The Bessel function in the integral can be integrated to give

$$P=2\pi eWLD_\perp n_0\kappa aJ_1(\kappa a)=7.84eWLD_\perp n_0\ \text{W}. \tag{11}$$

In this case, we see that the rf power depends on the length of the discharge but not on its radius; the radius cancels out because both the loss area and the gradient length are proportional to r.

The main problem is the calculation of $D_\perp$. For fractional ionizations greater than a few percent, electron–ion collisions are usually more important than electron–neutral collisions for electron transport. The diffusion then follows the rules for fully ionized, resistive plasmas. The diffusion in such plasmas is automatically ambipolar,[13] thus, a radial ambipolar electric field would not be expected. The classical diffusion coefficient D_c is proportional to the plasma density n, so that the profile of Eq. (9) would not be an accurate estimate; the diffusion problem is nonlinear. There is a more severe difficulty than this, how-

ever. Since, as we show later, the ions may have Larmor radii comparable to or larger than the tube radius, the usual formula

$$D_c=\eta_\perp n(KT_e+KT_i)/B^2 \tag{12}$$

is not valid; the ions' magnetic viscosity has to be taken into account. In this case, the diffusion is not ambipolar, and an inward radial electric field would be expected to arise. At the weakest fields it would be more sensible to assume straight ion orbits than to try to change D_c by adding the effect of viscosity. We shall use a modified treatment of ion-electron diffusion which is inexact but reasonable.

In weak discharges, collisions with neutral atoms dominate the transport mechanism. An electric field is set up to retard the radial loss of ions and enhance the loss of electrons. The net result is diffusion with the ambipolar coefficient[13]

$$D_{a\perp}=\frac{\mu_{i\perp}D_{e\perp}+\mu_{e\perp}D_{i\perp}}{\mu_{i\perp}+\mu_{e\perp}}\simeq D_{e\perp}+\frac{\mu_{e\perp}}{\mu_{i\perp}}D_{i\perp}, \tag{13}$$

where the approximation $\mu_{i\perp}\gg\mu_{e\perp}$ has been made, and

$$D_{e\perp}=\frac{KT_e\nu_e}{m\omega_c^2},\quad \mu_{e\perp}=\frac{e\nu_e}{m\omega_c^2}\quad(\omega_c^2/\nu_e^2\gg 1). \tag{14}$$

This is usually satisfied by two orders of magnitude even when the ions have small gyroradii. In that case, the $D_{i\perp}$ term is smaller than the $D_{e\perp}$ term by about T_i/T_e and usually can be neglected.

We can use Eq. (13) even when collisions with neutrals are infrequent if we use for ν_e the electron–ion collision frequency

$$\nu_{ei}=2.9\times10^{-12}\frac{n\ln\Lambda}{T_{\rm eV}^{3/2}}\ (\text{mks}). \tag{15}$$

When the ions have large gyroradii, they exchange momentum with the sheaths at the walls at each bounce and can be considered an independent fluid, since the momentum-conserving collisions with the electrons are no longer sufficient to couple the two fluids and ensure ambipolar diffusion. The question is the magnitude of the $D_{i\perp}$ term in Eq. (13). If the ions have nearly straight orbits, one should use $D_{i\parallel}$ instead, even if the value of $(\omega_{ci}/\nu_i)^2$ is large. Fortunately, it does not matter because the ratio D_i/μ_i is KT_i/e in either case. The last term in Eq. (13) is simply $D_{e\perp}(T_i/T_e)$. In practical units, both Eq. (12) and Eqs. (13)–(15) reduce to the result

$$D_{e\perp}=1.66\times10^{-2}\frac{n_{13}}{B_3^2}\frac{\ln\Lambda}{T_{\rm eV}^{1/2}}\left(1+\frac{T_i}{T_e}\right), \tag{16}$$

where n_{13} is density in units of 10^{13} cm^{-3} and B_3 is magnetic field in kG.

3. Ion temperature

Since the ion temperature has not been measured, we have calculated it in order to see the magnitudes of the ratios T_i/T_e and r_{Li}/a. The ions are heated by collisions with the electrons at the equilibration rate[14]

$$\nu_{\rm eq}=3.25\times10^{-15}\frac{n\ln\Lambda}{AT_{\rm eV}^{3/2}}\ (\text{mks}), \tag{17}$$

where A is the atomic number of the ions. They are cooled mainly by charge exchange collisions at the rate σv_i with the neutral atoms of temperature T_0, where $\nu_i=n_n\langle\sigma_{cx}v\rangle_i$, n_n being the neutral density. The charge exchange cross section σ_{cx} for argon is a function of T_i calculable from published data.[15] The equilibrium ion temperature is therefore described by

$$(T_e-T_i)\nu_{\rm eq}=(T_i-T_0)\nu_i(p,T_i), \tag{18}$$

where p is the neutral pressure. The ratio n/n_n can be expressed in terms of the fractional ionization F. Substituting the expressions for $\nu_{\rm eq}$ and ν_i, we can write Eq. (18) in the form

$$\frac{T_i}{T_e}=\frac{1+f(T_i)T_0T_e^{1/2}}{1+f(T_i)T_e^{3/2}}, \tag{19}$$

where

$$f(T_i)=1.27\times10^9(A/40)(\langle\sigma v\rangle/F), \tag{20}$$

A is the atomic number, $\langle\sigma v\rangle$ is in cm^3/s, and the temperatures are in eV. We have evaluated $\langle\sigma v\rangle(T_i)$ from charge exchange data and iterated Eq. (19) to obtain T_i as a function of T_e at a constant ionization fraction F of 10%. The result is shown in Fig. 5. For T_e around 3 eV, we see that T_i is about 0.07 eV. For magnetic fields of 100–1000 G, this gives ion Larmor radii of 2.4 cm to 2.4 mm for argon, spanning the range of tube radii used. Ions born at various potentials would gain energy from the electric field, leading to an energy spread of perhaps 0.25 eV. The ratio T_i/T_e is always small, however, so that that term can be neglected in Eq. (16).

4. Power scaling

If we use Eq. (16) for $D_\perp$ in Eq. (11), the required rf power in the case of radial losses only can be written

$$P=2\left(\frac{W}{200}\right)\left(\frac{n_{13}}{B_3}\right)^2L_{\rm cm}\ \text{W}, \tag{21}$$

where we have taken $\ln\Lambda=10$ and $T_e=3$ eV. This power depends on the length L of the discharge but is independent of the radius. Furthermore, for constant P, one would expect n/B to be constant as B is varied. Recalling that the helicon dispersion relation Eq. (3) also requires a constant ratio n/B, we see that, if radial losses are dominant, n/B can be cancelled between Eqs. (3) and (21) for helicon discharges, yielding a power level which depends only on geometry

$$P=40(L/a^2)_{\rm cm}\ \text{W}. \tag{22}$$

Here we have taken $W=200$ eV and $E_r=\frac{1}{2}mv_p^2=50$ eV. This simple relation is unfortunately not often valid, because axial losses are generally larger than radial losses in plasma processing applications. In Fig. 6, we plot both the axial and radial loss cases as given by Eqs. (7) and (21). Because of the different density scaling, the curves cross,

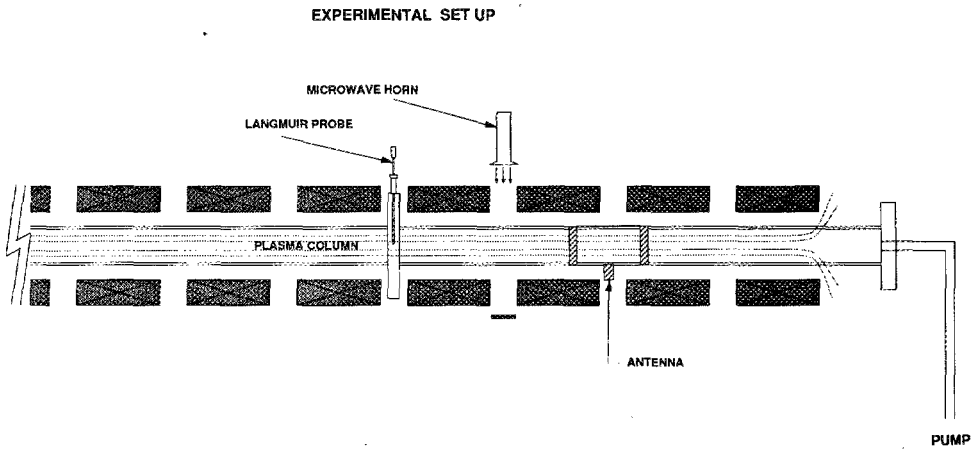

FIG. 7. Schematic of the apparatus.

and the higher curve at each density is the one that dominates. The highest density plasmas reported here have $n = (2\text{–}3) \times 10^{13}\ \text{cm}^{-3}$ with $a = 1\text{–}2$ cm, $L = 0.5\text{–}1.5$ m, and $B = 1$ kG. The curves cross for these parameters at $P \approx 1$ kW, so that both axial and radial losses are important. Although the power losses in the antenna and transmission line have not been accounted for, a power of 1 kW for each loss mechanism is consistent with the applied rf power of 2 kW.

III. EXPERIMENTS WITH 4-cm-DIAM TUBE

Figure 7 shows a schematic diagram of the apparatus. The quartz vacuum chamber has inside radius $a = 2$ cm and is 1.3 to 1.6 m long. It can be interrupted at one to four axial positions to accommodate probe ports; the data given here were taken with a single probe port at the position shown. The 12 magnetic field coils have the relative dimensions shown; the mounting flanges (not shown) leave 1.23 cm gaps between the coils for diagnostics. The resulting field is uniform to $\pm 5\%$ and can be raised to 1.3 kG. To avoid water cooling and damage to the probe, both the field and the rf are pulsed for $\leqslant 0.1$ s, with about 5% duty cycle. The two coils at each end are connected to a separate power supply so that the field shape can be controlled. The antenna's midplane is 25 cm from the probe.

The antenna is made of copper strip and configured as a Nagoya type III coil, except during tests of different antenna shapes. It is a half-wavelength, $m = 1$ antenna, usually 12 cm in length. It is driven with 2 kW from either a Henry Radio amplifier operating at 31.2 MHz, or an RF Plasma Products rf generator at 27.12 MHz. The relatively high frequency was dictated by the small tube diameters used, since the length of the antenna is set by the frequency and the resonant energy $\frac{1}{2}mv_p^2 = 50\text{–}200$ eV, and the antenna's aspect ratio is set by the tube diameter and the value of $k_\parallel/k_\perp$ needed for good coupling (Sec. II B). The matching circuit is a double-stub tuner made of 1.2-cm-diam rigid coax. The reflected power is monitored for each data point, and the circuit is retuned as necessary to keep the reflections under 1%; the reflected power is often much lower than this.

The Langmuir probe has a tungsten tip 0.5 mm in diam and 1.5 mm long. It is centered in its 1.6 mm (o.d.) alumina tube by a thin wrap of Ni foil spotwelded to the tungsten a few mm inside the tube; this prevents electrical contact with any conducting deposits that might form on the insulator. The latter is no longer than necessary to traverse the plasma diameter. As soon as possible after it enters the 6.3-mm-diam stainless steel probe shaft, the probe tip is connected to a small inductor whose *in situ* resonance frequency is near 30 MHz. Its impedance at resonance is in excess of 100 kΩ, ensuring that the probe potential follows space potential oscillations in the plasma at the rf frequency. Oscillations in saturation ion current have high output impedance and would not be filtered out,

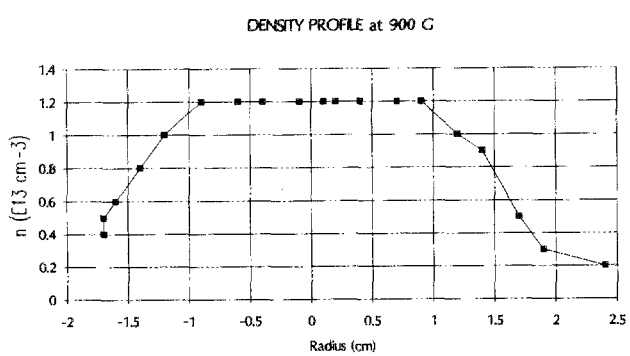

FIG. 8. Radial profile of plasma density with uniform magnetic field

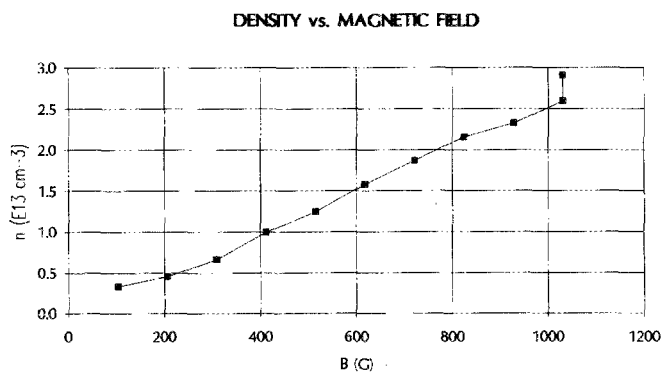

FIG. 9. Density vs magnetic field at high fields.

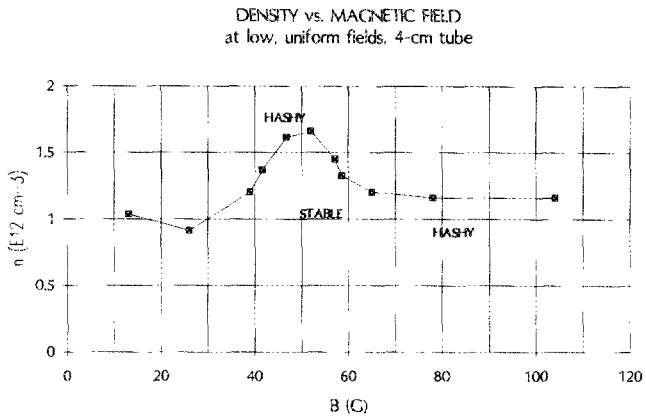

FIG. 10. Density vs magnetic field in the 50 G region.

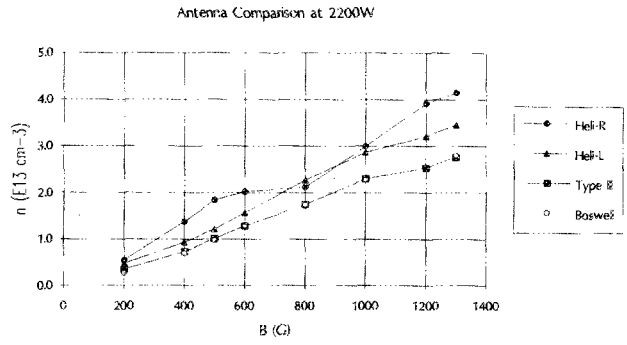

FIG. 12. Density vs magnetic field at $P = 2.2$ kW for four types of antennas: Nagoya type III, Boswell type, right-hand helical, and left-hand helical.

but they can be removed by a simple low-pass filter at the oscilloscope, since the probe's response to density fluctuations is linear. The discharge, however, is usually so quiescent that such filtering is unnecessary. For density measurements, the probe is biased to -125 V with a floating power supply (batteries); the 47 Ω measuring resistor is grounded at the oscilloscope. To avoid ground loops, all instrumentation is grounded at this one point. The plasma density is calculated from the formula

$$I_i = 0.5neA(KT_e/M)^{1/2}, \tag{23}$$

where I_i is the ion saturation current, and A is the probe tip's cylindrical area (since the ions have Larmor radii much larger than the probe diameter). The constant 0.5 is not exact, and the temperature T_e is not measured in every case, but the main uncertainty in the density measurements lies in the probe area A. Because of the jaggedness of the ceramic tube and the etching of the tungsten by ion sputtering, this area is uncertain by as much as 10%. Calibration of the probe with a 65 GHz microwave interferometer at the position shown in Fig. 7 gives agreement within this accuracy.

Figure 8 shows a typical density profile, taken at $B = 900$ G under standard conditions, which are as follows: $a = 2$ cm, $L = 130$ cm; $p = 4$ mTorr of argon; $P_{rf} = 2.2$ kW; half-wavelength Nagoya type III antenna, 12 cm long; uniform magnetic field. All data can be assumed to be taken under these conditions unless otherwise specified. The profile of Fig. 8 is extremely flat over the central 2 cm of the 4 cm diameter. The small density past $r = 2$ cm on the right is due to the diffusion of plasma into the probe port. The flatness of the profile is entirely consistent with the anticipated[6] energy deposition profile, which has a maximum at $r/a = 0.48$.

Figure 9 shows variation of density with magnetic field using the standard antenna. The curve is approximately linear at high fields. Below about 200 G, the matching

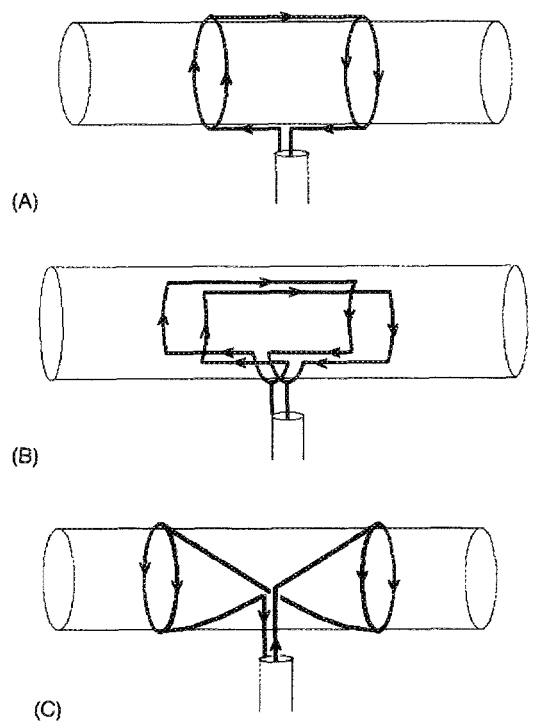

FIG. 11. Half-wavelength, $m = 1$ antenna configurations: (a) Nagoya type III, (b) Boswell type, and (c) Shoji (helical) type.

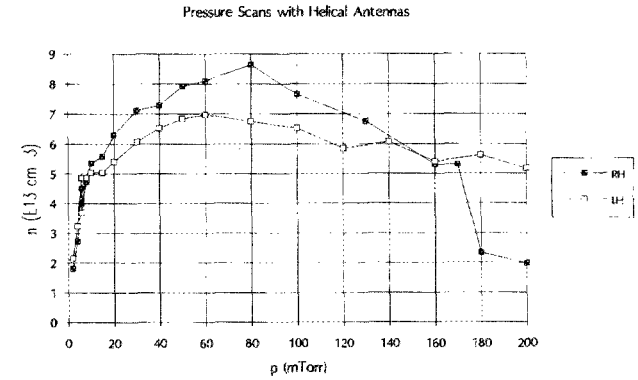

FIG. 13. Density vs pressure (in mTorr) for right- and left-hand helical antennas.

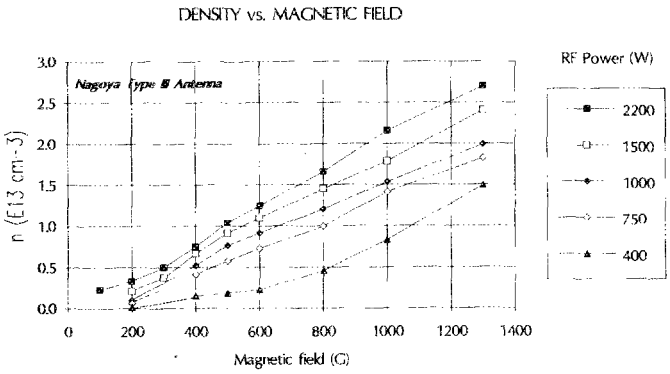

FIG. 14. Density vs magnetic field for antenna (A) at various rf powers.

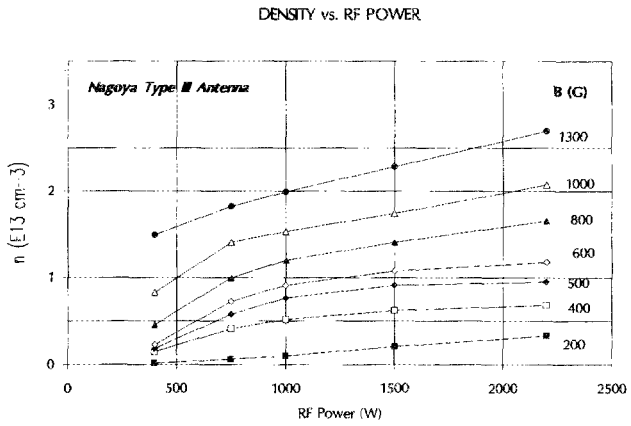

FIG. 16. Density vs rf power for the Nagoya type III antenna.

circuit usually had to be considerably retuned, showing that the plasma impedance changes there. The low field region is shown in Fig. 10; a distinct mode change is seen in the discharge here. A very stable discharge is obtained at 50 G, surrounded by hashy regions of mode switching on either side. The discharge is extremely noisy, with 100% density fluctuations, below 20 G. We have explained the low-field peak as a second root of the helicon dispersion relation, found when the second term in the denominator of Eq. (1), due to electron inertia, is retained.[16] This mode is essentially a Trivelpiece–Gould electron cyclotron wave in a finite cylinder. The frequency is approximately $\omega = \omega_c \cos\theta$, where $\cos\theta = k_\parallel/k$. Taking $k_\perp \approx k \approx 3.83/a$ and $k_\parallel = \pi/L_a$, where the antenna length L_a is 12 cm, we find that the mode should occur at 71 G. Conversely, a 50 G resonance would imply a parallel wavelength of 17 cm. The difference from the expected wavelength of $2L_a = 24$ cm is not worrisome, since the antenna can excite a wide spectrum of wavelengths, and, as we shall see later, indeed does.

The low-field mode offers the possibility of producing an ECR discharge in the $n = 10^{12}$ cm^{-3} range using 13.56 MHz rather than 2.45 GHz. The advantages would be the economy gained in using tens of gauss rather than 875 G, and in the more uniform plasmas expected with the larger Larmor radii. The Landau damping mechanism is the same for both roots of the dispersion relation. We have not yet explored this mode in detail.

We now turn our attention to the dense plasmas produced at high fields. Four antenna configurations have been used; these are shown in Fig. 11. Antenna (A) is the standard one we have used. Antenna (B) is an approximation to the one preferred by Boswell.[5] The essential point is that the top and bottom current paths of antenna (A) have been divided into two separated paths, thus perhaps producing a field that matches better to the wide pattern of Fig. 2. Antenna (C) has two versions of opposite helicity. Since the antenna is located near one end of the chamber, waves propagating toward the far end have a greater effect on ionization. This asymmetry causes one helicity to produce preferentially right-hand circularly polarized waves; and the other, the opposite polarization.

The following data were taken with the two end coils in Fig. 7 turned off; the reason for this will be revealed later. Figure 12 shows the n–B curve for four antennas, (A), (B), (C), and (C′), at the highest available power. Considering first the Nagoya type III and Boswell antennas, we see that they are essentially identical. Figures 14 and 15 show the n-B curves for these antennas as the rf power is varied. Above about 500 W and 500 G, the value of n/B is approximately constant, as expected from the helicon dispersion relation, Eq. (3). These curves do not in them-

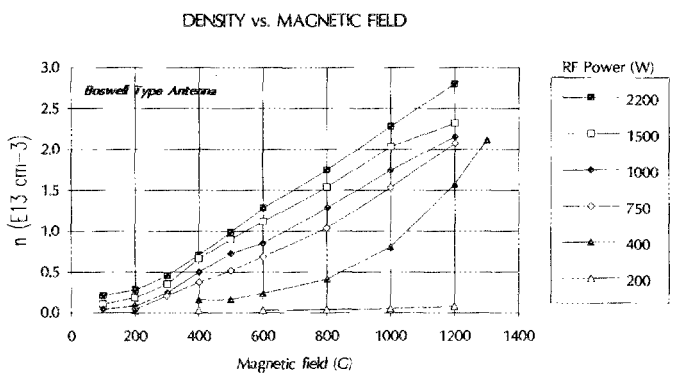

FIG. 15. Density vs magnetic field for antenna (B) at various rf powers.

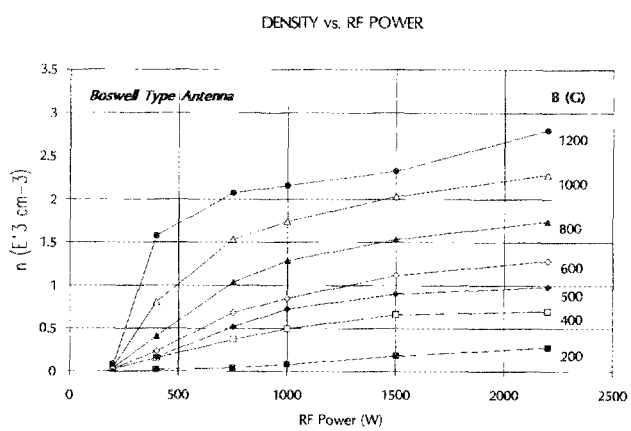

FIG. 17. Density vs rf power for the Boswell type antenna.

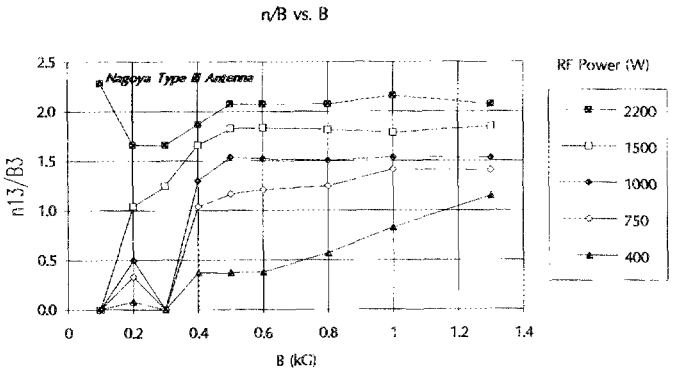

FIG. 18. Measured ratios of n/B for the Nagoya type III antenna. Here the density n_{13} is in units of 10^{13} cm $^{-3}$ and the field B_3 is in kG.

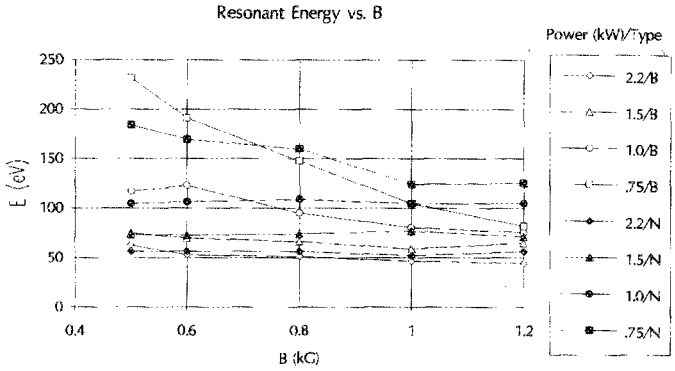

FIG. 20. The electron energy E corresponding to the phase velocity, as computed from measured values of n/B, as a function of magnetic field and rf power. The open points are for the Boswell antenna (B); the solid points for the Nagoya type III antenna (N).

selves imply agreement with helicon wave theory, because radial diffusion scaling, Eq. (21), also implies a constant n/B ratio. However, Fig. 6 shows that axial diffusion should be dominant under these conditions; furthermore, it will be seen that the value of n/B is in agreement with the dispersion of helicon waves. The two helical antennas can be seen to give densities higher than either of the plane-polarized antennas, contrary to expectation. The L-helical antenna, whose helicity would excite left-hand circularly polarized waves propagating from the antenna to the probe, gives quiescent discharges at almost all magnetic fields. The R-helical antenna creates even higher densities at the highest fields, but the curve is not smooth because unstable operation is encountered at almost all fields, with the discharge switching modes during the pulse. We believe that the R-helical antenna was so efficient that it was starved for gas. Indeed, as shown in Fig. 13, at higher pressures the instability is quenched, and the density approaches 10^{14} cm $^{-3}$.

Figures 16 and 17 show the variation of density with rf power at various B fields for antennas (A) and (B), respectively. At 200 W, the discharge barely ignites, and above about 500 G it is fully established. The density depends more on magnetic field than on power.

From the data of Figs. 14 and 15, we can plot the ratio n/B versus magnetic field for various powers; this is shown in Figs. 18 and 19 for antennas (A) and (B). As before, we see that above about 500 G and 500 W the value of n/B is essentially constant, especially for the standard antenna. From these values of n/B we can compute the corresponding resonant energy $E_r = \frac{1}{2}mv_p^2$ from Eq. (3). For this calculation, we have included the first-order correction to the approximate value $k_\perp = 3.83/a$, as given by Eq. (41) of Ref. 6. This works out to be

$$E_r(\text{eV}) = \left(\frac{32.1}{a}\frac{B_3}{n_{13}} - 7.2f_9\right), \tag{24}$$

where a is in cm and f_9 is the rf frequency in GHz. The result is shown in Fig. 20. It is apparent that at high fields and powers, the values of n/B correspond to resonant energies between 50 and 100 eV. This corresponds well with the region of maximum ionization cross section.[17]

A surprising increase in density occurred when the magnetic field was made nonuniform by turning off the end coils. The field lines near the antenna then had the shape shown in Fig. 21. The increase in density under standard conditions with change in the end coil current is shown in Fig. 22. When the end coils were turned off, the density increased by more than a factor of 3. When the end coil current was reversed, forming a cusp, the density increased further, finally saturating at about a factor of 5 over the uniform field case. The radial density profile with reversed end coils is shown in Fig. 23. The profile is noticeably narrower than before, and this could also be seen visually.

The observation of a bright, fully ionized core at high rf powers has been reported by both Boswell and Shoji (private communication). This does not occur in our experi-

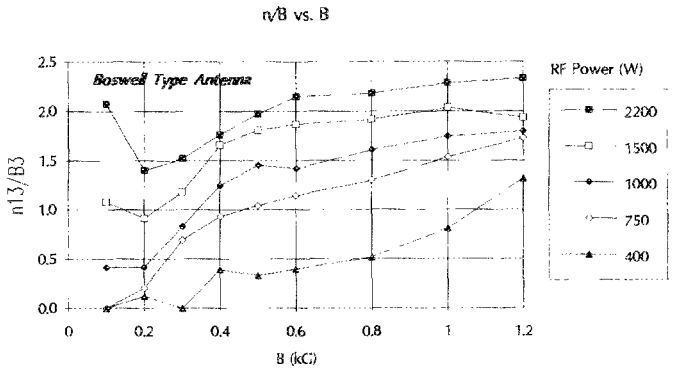

FIG. 19. Measured ratios of n/B for the Boswell type antenna.

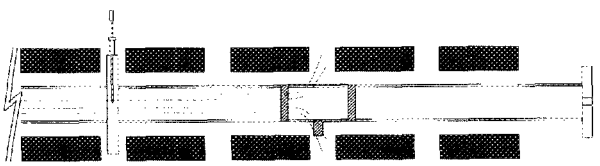

FIG. 21. Magnetic field line configuration with the end coils off.

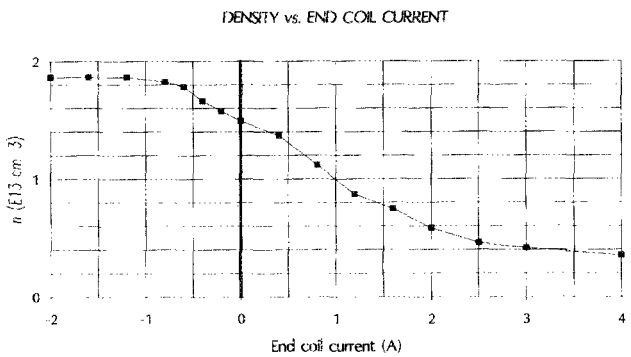

FIG. 22. Variation of density with end coil current. The main magnetic field was 560 G. Negative currents are opposite to those in the main coils. A positive current of about 6 A would give a uniform field. Zero indicates the end coils off condition used in taking most of the data at high fields.

ment with a uniform field, but apparently we have been able to reproduce a similar condition with a nonuniform field. We do not understand what is happening in the other experiments, which differ from ours mainly in the use of a lower frequency (7 MHz), but we surmise that the following happens in our case: The cusp field brings the off-axis plasma quickly to the walls, acting as a magnetic limiter to the plasma radius. Since the absorption of helicon waves can occur only where n/B has the right value, the rf power is then concentrated into a smaller volume of plasma. The same efficiency cannot be achieved by using a smaller tube radius, because the large-orbit primary electrons will run into the walls. By using an aperture limiter, the power can be concentrated in a small column without losing the primaries.

We have also investigated the effect of varying the length of the Nagoya type III antenna. The standard length of 12 cm corresponds to a resonant energy of 120 eV; that is, it preferentially excites waves with a phase velocity v_p such that $\frac{1}{2}mv_p^2 = 120$ eV. The n–B curve for a 20 cm antenna, with $E_r = 335$ eV, is shown in Fig. 24 for various end coil conditions. The same for a 7.7 cm antenna, with $E_r = 50$ eV, is shown in Fig. 25, in comparison with the 12 cm antenna results at 1 kG. All three antennas are compared in Fig. 26 in the "end coil off" condition. It is seen that the standard 12 cm antenna gives the best density. For shorter antennas of this diameter, the value of

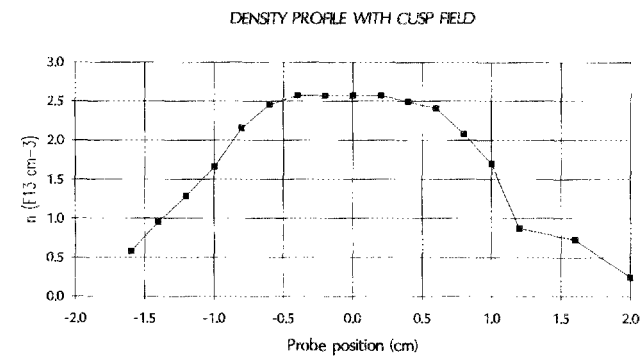

FIG. 23. Density profile with reversed end coil current.

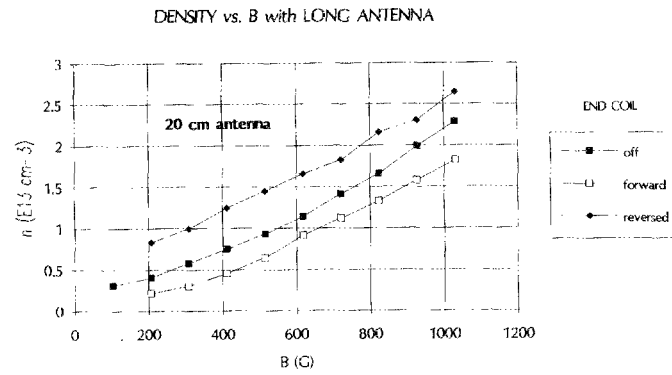

FIG. 24. Density vs magnetic field for a 20 cm long Nagoya type III antenna, with different field shapes.

$k_\perp/k_\parallel$ is too small to give good electrostatic coupling; for longer antennas, the resonant energy is too high for efficient ionization.

IV. EXPERIMENTS WITH 2-cm-DIAM TUBE

Though these experiments preceded those on the 4 cm tube, the results are so complex that they can be fully understood only after further work. We have used four configurations. The first is a 90 cm long machine, the same as shown in Fig. 7 except that the vacuum tube extends an equal distance on either side of the probe; a diagram has been shown previously.[18] This device could not be operated at high fields because of the onset of relaxation oscillations.[19] This can be understood qualitatively from Eq. (3), which shows that for smaller a, the value of n/B has to be larger. Since radial losses also increase with smaller tube radius, the available power was apparently insufficient to produce the proper density for the helicon resonance except at low magnetic fields. Figure 27 shows typical density and potential profiles at a field of about 100 G. Note that the radial electric field is in the direction for confining electrons, not ions. Figure 28 shows a typical density-magnetic field plot; the linear regime exists only

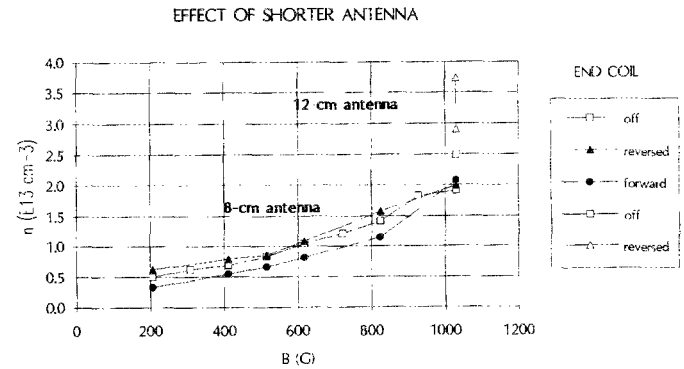

FIG. 25. Density vs magnetic field for a 7.7 cm long Nagoya type III antenna, with different field shapes. Data for the 12 cm antenna at the highest field are given for comparison. The relative insensitivity of the 7.7 cm antenna to field shape may be due to the fact that this antenna was fed from the end rather than from the center, and the antenna lay entirely within the last normal coil.

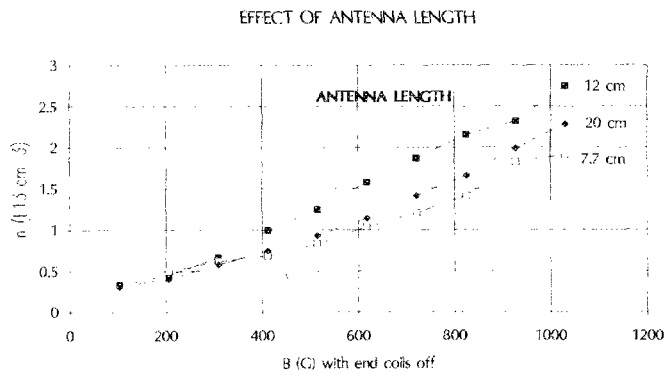

FIG. 26. Comparison of the n–B curves for 7.7, 12, and 20 cm antennas with the end coils off.

between 40 and 100 G. At higher fields, the discharge is turbulent and no longer supports a helicon wave. At low fields, a large cyclotron peak can be seen.

The discharge is sensitive to the end boundaries. We first noticed this when we tried to insert probes and collectors from the end. The nature of the discharge changed upon introduction of these collectors and even of simply a grounded probe shaft that was withdrawn almost to the back plate. In Fig. 29 we show the effect on the n–B curve of (A) a large tantalum endplate covering the whole diameter, and (B) a small (5 mm diam) endplate. In Fig. 30 we see that a split plate caused visible changes in the plasma depending on how it was grounded. When both parts (A) and (B) of the plate were floating, the discharge did not reach the end of the machine. When both were grounded, the discharge reached the end but was noticeably fainter there than near the antenna. When only the center was grounded, a very bright discharge extended uniformly to the end. Biasing the endplate segments did not produce other modes, and the results were not understandable. We surmise that end electrodes on the axis are connected to the highly conducting plasma so as to make the plasma into a coaxial transmission line. When the central field lines are charged positive relative to those on the outside, the radial electric field helps to confine energetic elec-

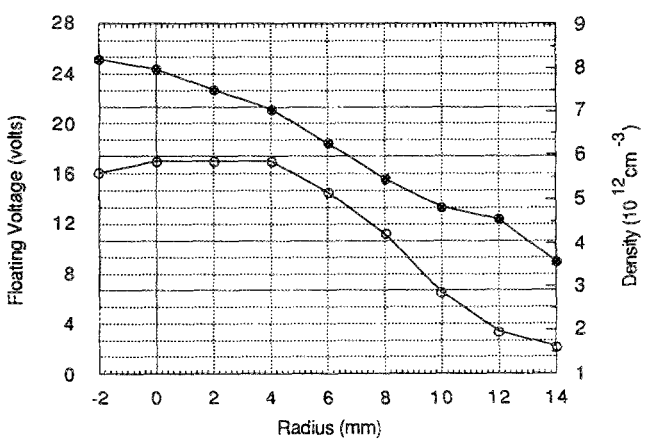

FIG. 27. Radial profiles of density (solid points) and probe floating voltage (open points) at the midplane of a 90 cm long, 2-cm-diam discharge.

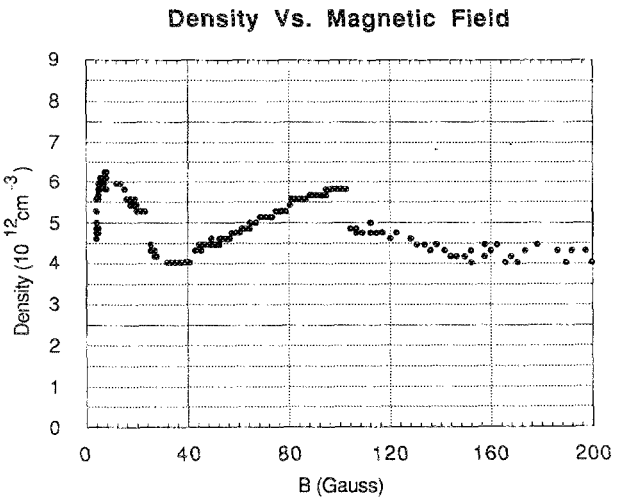

FIG. 28. Density vs magnetic field for the 2-cm-diam discharge under standard conditions (4 mTorr of argon, 1600 W rf power).

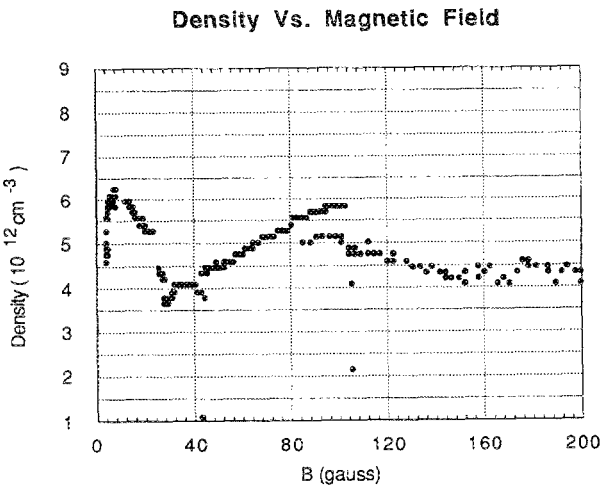

(A)

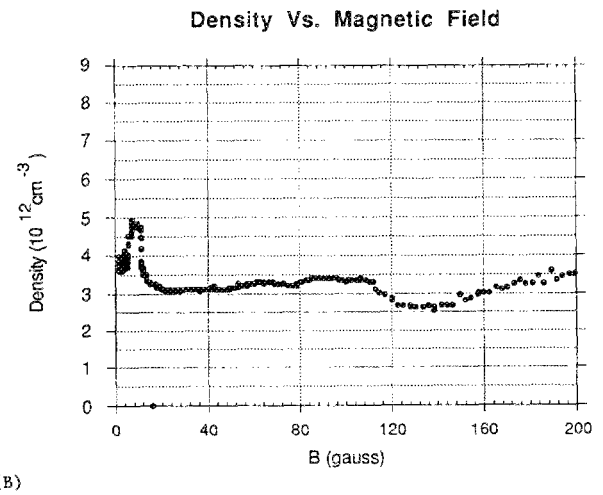

(B)

FIG. 29. The n-B curve when the discharge was terminated by (A) a large endplate, and (B) a small endplate.

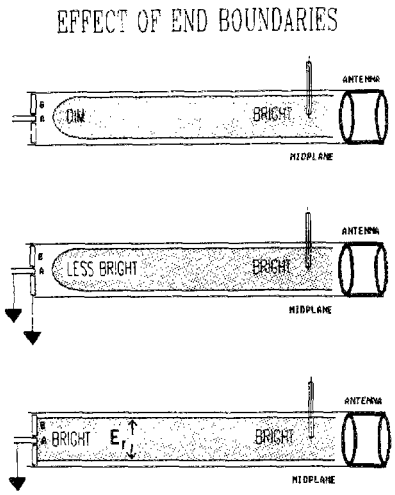

FIG. 30. Changes in the appearance of the plasma caused by grounding the inner (A) or outer (B) parts of a split endplate.

trons which have Larmor orbits as large as the tube radius, as discussed in the next paragraph.

When the floating potential of a large endplate is monitored as the magnetic field is swept, a sudden jump was found to occur reproducibly when the field reached 25–40 G (Fig. 31). The endplate voltage sometimes was as high as 200 V negative. That this voltage is not simply a rectification of the rf field was verified by moving the endplate toward the antenna. The magnitude of the potential *decreases* towards the antenna. These observations are consistent with the picture[18] that fast electrons are accelerated by the longitudinal electric field of the helicon wave and gain energy as they move away from the antenna. By scattering elastically, these primary electrons gain large Larmor orbits and eventually strike the wall. The loss of a fraction of the primaries at low fields causes the jump in potential seen in Fig. 31. The 25–40 G at which the potential jump occurs corresponds to an electron energy of 50–

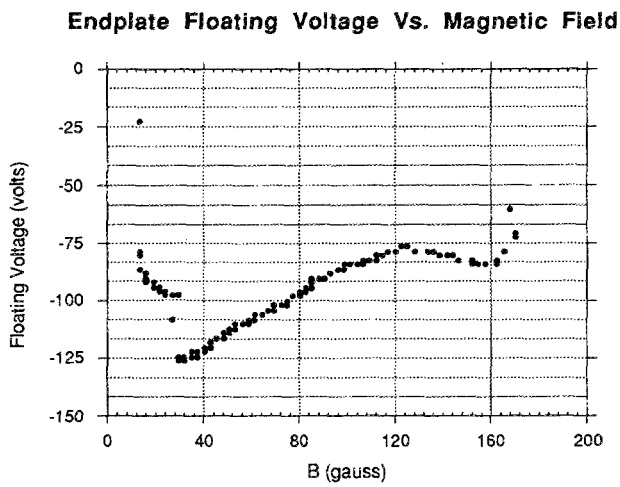

FIG. 31. The floating potential of a large endplate vs magnetic field.

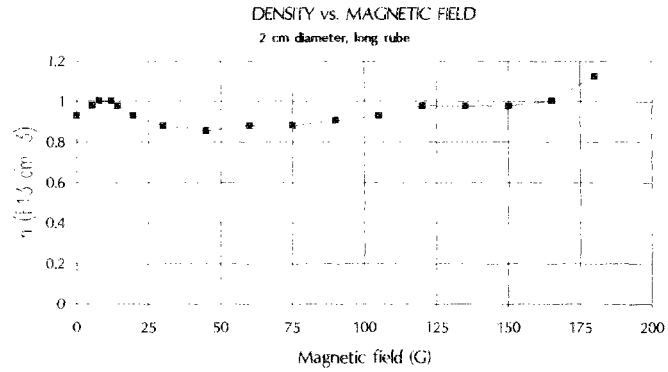

FIG. 32. The n–B curve for 2-cm-diam discharges in a long, uniform B field.

150 eV, exactly at the peak of the argon ionization cross section.

The second configuration used with the 2-cm-diam tube was with a uniform field 1.5 m long, as in Fig. 7. Figure 32 shows the low magnetic field region of the n–B curve. The cyclotron peak is small, and the density is modest. In the third configuration, a long tube was used, but the magnetic field was imposed over only half of it. In this case, the field lines diverged to the wall at the end away from the antenna, and the discharge achieved a somewhat higher density, shown in Fig. 33. It was turbulent above about 200 G but was quiescent and extended to the end, through the field-free region, at fields between 50 and 150 G. At the low-field peak the discharge extended only so far as the magnetic field did. The region below 50 G is explored further in Fig. 34. There is a very quiescent discharge around 35 G, and the plasma becomes very noisy below 10 G. As the field is swept, one always notices a point at which the reflected rf power becomes extremely low, indicating good coupling to the plasma; however, this point is not related to any increase in density. The increase of density with rf power is shown in Fig. 35. The curve does not saturate at 2 kW, indicating that higher magnetic fields could be used if more power were available.

Finally, in the fourth configuration, the coils in one half of the machine were removed, and the vacuum chamber

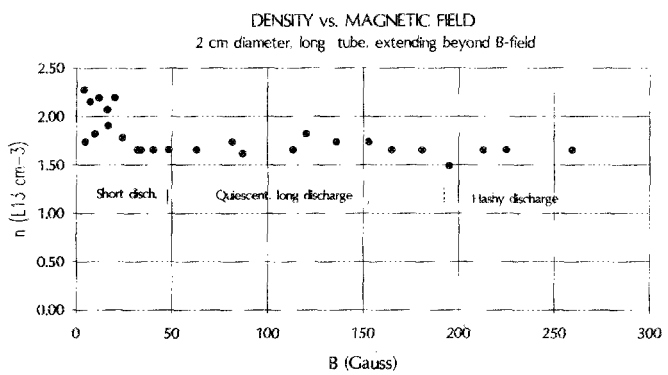

FIG. 33. The n–B curve for 2-cm-diam discharges in a long tube with a short B field.

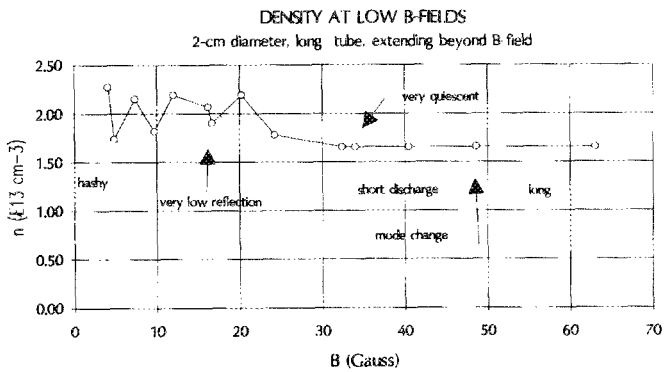

FIG. 34. The n–B curve for 2-cm-diam discharges at very low B fields.

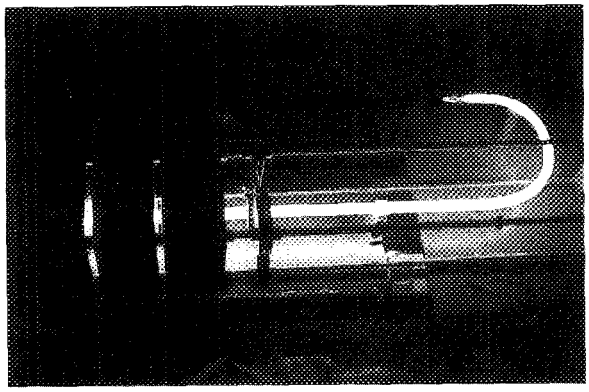

FIG. 36. Photograph of a helicon discharge propagating outside of the magnetic field region.

was bent into a U bend. At fields above 75 G or so, the discharge extended beyond the last coil and around the U bend. The discharge lost intensity away from the antenna, but it was bright even at the very end, as seen in Fig. 36. In the field-free region, helicon waves cannot exist, and only two slow waves in the plasma are possible: ion acoustic waves and electron plasma waves. The frequency is too low for plasma waves, and ion waves at this frequency would have too short a damping length. There are two possibilities for this behavior. First, the helicon waves are mode-converted to surface waves, which can propagate in the field-free region. Second, the primaries are produced in the magnetized region, and these are electrostatically trapped by sheaths on the walls as they go around the U bend. In this case, helicon discharges in small tubes would take on some of the characteristics of capillary discharges and fluorescent lights.

V. SUMMARY

Data taken with 4-cm-diam tubes show that the density-magnetic field ratio is consistent with helicon acceleration of electrons to energies where the argon ionization cross section has a maximum. An unexpected finding is the five-fold increase in density when a cusp field is applied near the antenna. Data taken with 2-cm-diam tubes give evidence of wave acceleration of primary electrons, but show the importance of electrostatic charges on the tube walls on the discharge characteristics. Furthermore, the size of the Larmor orbits of the fast electrons is comparable to the tube radius, thus introducing another critical length into the analysis of the equilibrium. These two effects make small-bore helicon discharges extremely difficult to understand quantitatively. With both diameters, we have found a density peak at fields of tens of Gauss, which we attribute to a bounded electron cyclotron mode. Further exploration of this mode can lead to radiofrequency ECR discharges, which could be more economical and uniform than microwave ECR plasma generators.

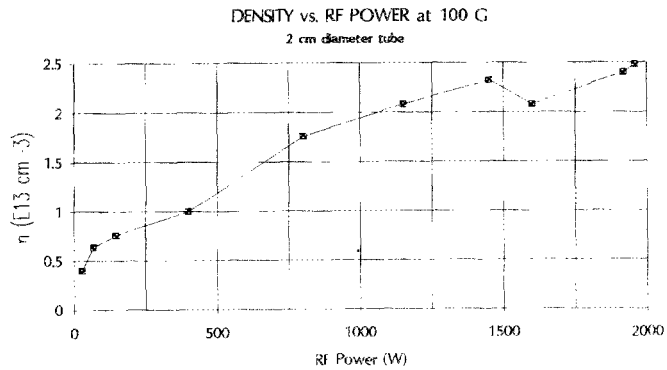

FIG. 35. Density vs rf power for 2-cm-diam discharges at 100 G.

ACKNOWLEDGMENTS

This work was supported by the National Science Foundation, Grant No. ECS 8901249. We are grateful to G. Chevalier, M. Light, and C. Decker for collaboration on the experiment, and to the RF Plasma Products, Inc., for the loan of a unique 27.12 MHz, 2.2 kW rf generator.

[1] R. W. Boswell, Plasma Phys. Controlled Fusion **26**, 1147 (1984).
[2] A. J. Perry and R. W. Boswell, Appl. Phys. Lett. **55**, 148 (1989).
[3] P. Zhu and R. W. Boswell, Phys. Rev. Lett. **63**, 2805 (1989).
[4] R. W. Boswell, A. J. Perry, and M. Emami, J. Vac. Sci. Technol. A 7, 3345 (1989).
[5] P. Zhu and R. W. Boswell, Phys. Fluids B **3**, 869 (1991).
[6] F. F. Chen, Plasma Phys. Controlled Fusion **33**, 339 (1991).
[7] A. Komori, T. Shoji, K. Miyamoto, J. Kawai, and Y. Kawai, Phys. Fluids B **3**, 893 (1991).
[8] P. K. Loewenhardt, B. D. Blackwell, R. W. Boswell, G. D. Conway, and S. M. Hamberger, Phys. Rev. Lett. **67**, 2792 (1991).
[9] T. Watari *et al.*, Phys. Fluids **21**, 2076 (1978).
[10] F. F. Chen, TRW Report Task-II-3552 (unpublished).
[11] B. McVey, TRW Report Task-II-2740 (unpublished).
[12] F. F. Chen, Bull. Am. Phys. Soc. **35**, 2101 (1990).
[13] F. F. Chen, *Introduction to Plasma Physics and Controlled Fusion*, 2nd ed. (Plenum, New York, 1984), Vol. 1, Chap. 5.
[14] D. L. Book, NRL Publication 0084-4040, 1987.
[15] J. W. Sheldon, Phys. Rev. Lett. **8**, 64 (1962).
[16] F. F. Chen and C. D. Decker, Bull. Am. Phys. Soc. **34**, 2128 (1989).
[17] D. Rapp and P. Englander-Golden, J. Chem. Phys. **43**, 1464 (1965).
[18] F. F. Chen and C. D. Decker, (to be published).
[19] F. F. Chen, Lasers Particle Beams **7**, 551 (1989).

Erratum

Eq. (24): $E_r(\text{eV}) = \left(\frac{32.1}{a} \frac{B_3}{n_{13}} - 7.2 a f_9 \right)^2$